

# Green Chemistry

Accepted Manuscript



This is an *Accepted Manuscript*, which has been through the Royal Society of Chemistry peer review process and has been accepted for publication.

*Accepted Manuscripts* are published online shortly after acceptance, before technical editing, formatting and proof reading. Using this free service, authors can make their results available to the community, in citable form, before we publish the edited article. We will replace this *Accepted Manuscript* with the edited and formatted *Advance Article* as soon as it is available.

You can find more information about *Accepted Manuscripts* in the [Information for Authors](#).

Please note that technical editing may introduce minor changes to the text and/or graphics, which may alter content. The journal's standard [Terms & Conditions](#) and the [Ethical guidelines](#) still apply. In no event shall the Royal Society of Chemistry be held responsible for any errors or omissions in this *Accepted Manuscript* or any consequences arising from the use of any information it contains.



Journal Name

ARTICLE

## Photocatalytic reduction of CO<sub>2</sub> with H<sub>2</sub>O to CH<sub>4</sub> over ultrathin SnNb<sub>2</sub>O<sub>6</sub> 2D nanosheets under visible light irradiation

Shuying Zhu,<sup>a</sup> Shijing Liang,<sup>a,b,c\*</sup> Jinhong Bi,<sup>a,b</sup> Minghua Liu,<sup>a,b</sup> Limin Zhou,<sup>c</sup> Ling Wu<sup>a</sup> and Xuxu Wang<sup>a\*</sup>

Received 00th January 20xx,  
Accepted 00th January 20xx

DOI: 10.1039/x0xx00000x

www.rsc.org/

Monolayer SnNb<sub>2</sub>O<sub>6</sub> two-dimensional (2D) nanosheets with high crystallinity are prepared by one-pot and eco-friendly hydrothermal method without any organic additive. For the first time, these SnNb<sub>2</sub>O<sub>6</sub> nanosheets are applied into the photocatalytic reduction of CO<sub>2</sub> with H<sub>2</sub>O to CH<sub>4</sub> in the absence of co-catalysts and sacrificial agents under visible light irradiation. The structure features, morphology, photoabsorption performance, and photoelectric response have been investigated in detail. Results show the as-prepared SnNb<sub>2</sub>O<sub>6</sub> samples with typical 2D nanosheet in the thickness of about 1 nm. Owing to the unique features of the nanosheets, the surface area, photoelectrical property and the surface basicity of SnNb<sub>2</sub>O<sub>6</sub> are greatly improved compared with the counterpart prepared by traditional solid state reaction. Furthermore, the adsorption capacity of CO<sub>2</sub> on SnNb<sub>2</sub>O<sub>6</sub> nanosheets is much higher than that of layered SnNb<sub>2</sub>O<sub>6</sub>. Thus, the photocatalytic activity of SnNb<sub>2</sub>O<sub>6</sub> nanosheets for the reduction of CO<sub>2</sub> is about 45 and 4 times higher than those of the references (layered SnNb<sub>2</sub>O<sub>6</sub> and common N-doped TiO<sub>2</sub>), respectively. To understand the interaction between the CO<sub>2</sub> molecule and the surface of photocatalyst, and the reactive species in the reduction process, the intermediates have also been detected by in situ FTIR with and without visible light irradiation. Finally, a possible mechanism for the photocatalytic reduction of CO<sub>2</sub> with H<sub>2</sub>O to CH<sub>4</sub> on SnNb<sub>2</sub>O<sub>6</sub> nanosheet is proposed. We believe this work will provide new opportunities for enlarging the family of visible-light driven photocatalysts for the reduction of CO<sub>2</sub>.

### 1. Introduction

The idea of mimicking natural photosynthetic cycle of the chemical conversion of CO<sub>2</sub> into useful fuels, such as methane, formic acid, and methanol, has been consistently gaining attention.<sup>1-5</sup> Such artificial photosynthesis allows the direct conversion of CO<sub>2</sub> into valuable compounds using sunlight at room temperature and ambient pressure in order to reduce atmospheric CO<sub>2</sub> concentrations while providing renewable carbon fixation and energy storage. Yet, to date, the overall photoconversion efficiency is still very low and requires further promotion for commercialization. The key factor to address this issue is the development of efficient photocatalyst.

Recently, many inorganic semiconductor materials (such as NaNbO<sub>3</sub>,<sup>6</sup> ZnGe<sub>2</sub>O<sub>4</sub>,<sup>7</sup> ZnGa<sub>2</sub>O<sub>4</sub>,<sup>8</sup> CdS,<sup>9</sup> TiO<sub>2</sub><sup>10-14</sup> and Cu<sub>x</sub>Ag<sub>y</sub>In<sub>z</sub>Zn<sub>k</sub>S<sub>m</sub> solid solution<sup>15</sup>) are exploited as photocatalysts for the reduction of CO<sub>2</sub>. Meanwhile, some organic semiconductors (such as g-C<sub>3</sub>N<sub>4</sub><sup>16-19</sup> and metal organic

frameworks (MOFs)<sup>20-22</sup>) and some non-semiconductors (such as zeolite molecular sieve<sup>23, 24</sup> and layered double hydroxides<sup>25</sup>) have also been developed. Furthermore, the dye-sensitization,<sup>26-28</sup> precious metal modification<sup>29</sup> and the co-catalyst loading<sup>30, 31</sup> are used for the enhancement of the photocatalytic activity. However, sustainable utilization of solar energy by the reduction of CO<sub>2</sub> calls for the development of more abundant and stable catalysts working with visible light, and this has remained challenging so far.<sup>32</sup> It is due to the facts that (1) most of developed inorganic photocatalysts are stable but just activated by UV light; (2) the organic photocatalysts suffer from high charge carrier recombination rates, poor activity and stability, and rigorous syntheses conditions; (3) the weak interaction between CO<sub>2</sub> molecules and the surface of photocatalysts reduce the mass transfer of CO<sub>2</sub>; (4) some visible light driven photocatalysts contain the highly toxic heavy metal element.

SnNb<sub>2</sub>O<sub>6</sub>, a typical layered semiconductor material, is constructed by numbers of SnNb<sub>2</sub>O<sub>6</sub> sheets and has been used as photocatalyst into water splitting and the degradation of organic pollutants.<sup>33-37</sup> The SnNb<sub>2</sub>O<sub>6</sub> sheet consists of a polyanion layer built by corner-sharing NbO<sub>6</sub> octahedra flat and edge-sharing Sn<sup>II</sup>O<sub>8</sub> square antiprisms flat.<sup>38</sup> The thickness of monolayer SnNb<sub>2</sub>O<sub>6</sub> is only 0.85 nm. Thus, the formation of photogenerated charge carrier could be mobilized and separated rapidly from the interior of the sheet to the surface to participate in the reaction. Furthermore, the surface

<sup>a</sup> State Key Laboratory of Photocatalysis on Energy and Environment, Fuzhou University, Fuzhou 350002, P. R. China.

<sup>b</sup> Department of Environmental Science and Engineering, Fuzhou University, Minhou, Fujian, 350108, P. R. China.

<sup>c</sup> Department of Mechanical Engineering, The Hong Kong Polytechnic University, Hung Hom, Kowloon, Hong Kong

† Footnotes relating to the title and/or authors should appear here.

Electronic Supplementary Information (ESI) available: [details of any supplementary information available should be included here]. See DOI: 10.1039/x0xx00000x

exposed Sn<sup>II</sup> ions with rich electron have been considered as a strong Lewis basic, which could serve as the sites to chemically adsorb CO<sub>2</sub> (Lewis acid) by an acid-basic interaction. And then, the inert CO<sub>2</sub> molecules would be activated. This is a very important step in the reduction of CO<sub>2</sub>.<sup>14</sup> Notably, metal ions in SnNb<sub>2</sub>O<sub>6</sub> are eco-friendly and earth abundant. Therefore, it seems that SnNb<sub>2</sub>O<sub>6</sub> would be a potential photocatalyst for efficient reduction of CO<sub>2</sub>. However, the study on the reduction of CO<sub>2</sub> over SnNb<sub>2</sub>O<sub>6</sub> has not been reported. It may be due to the fact that the high charge density of the inner sheets in layer and small interlamellar spacing result in difficulty associated with the intercalation of reactant molecules. So the layered SnNb<sub>2</sub>O<sub>6</sub> exhibited the poor activities due to the lack of active site on the external surface of the catalyst. In the previous work, we have prepared monolayer SnNb<sub>2</sub>O<sub>6</sub> nanosheet photocatalyst by hydrothermal reaction and microwave-assist hydrothermal reaction.<sup>36, 37</sup> It was found that the nanosheet exhibited a greatly increased photocatalytic activity in the degradation of organic pollutants. Furthermore, the 2D nanosheet configuration can provide a large fraction of exposed surface metal sites due to its surface effects.<sup>39</sup> The 2D sheet geometry facilitates the adsorption of reactants and desorption of products. Therefore, it is interesting to investigate the reduction of CO<sub>2</sub> over SnNb<sub>2</sub>O<sub>6</sub> nanosheet. This not only widens the application of the 2D nanosheet, but also promotes the development of efficient photocatalysts for the reduction of CO<sub>2</sub> into the fuels.

Herein, monolayer SnNb<sub>2</sub>O<sub>6</sub> 2D nanosheets have been prepared by a simple and eco-friendly hydrothermal reaction without any organic additive. The physicochemical properties of SnNb<sub>2</sub>O<sub>6</sub> 2D nanosheets were characterized in detail. On the basis of the structural features of SnNb<sub>2</sub>O<sub>6</sub> 2D nanosheets, the photocatalytic reduction of CO<sub>2</sub> over the nanosheets was investigated for the first time. The layered SnNb<sub>2</sub>O<sub>6</sub> and N-doped TiO<sub>2</sub> were taken as references. To understand the reasons for the enhanced photocatalytic activity of SnNb<sub>2</sub>O<sub>6</sub> 2D nanosheets, the photoelectric property, the CO<sub>2</sub> adsorption capability, and the interaction between CO<sub>2</sub> and the nanosheets have been studied in detail. Finally, a possible mechanism for the photocatalytic reduction of CO<sub>2</sub> to CH<sub>4</sub> on SnNb<sub>2</sub>O<sub>6</sub> nanosheet was proposed.

## 2. Experimental

### 2.1. Preparation of catalysts

The SnNb<sub>2</sub>O<sub>6</sub> (SN) was prepared by a facile hydrothermal (HT) reaction following a simple procedure we reported previously.<sup>37</sup> Briefly, the mixture of the self-prepared Nb<sub>2</sub>O<sub>5</sub>·nH<sub>2</sub>O and SnCl<sub>2</sub> in a molar ratio of Nb<sup>5+</sup>: Sn<sup>2+</sup> = 2: 1 was dispersed into 70 mL deionized water, and then was transferred to a 100 mL Teflon-lined stainless steel autoclave. After that, the pH values were adjusted by 4 mol L<sup>-1</sup> NaOH under vigorous stirring. Subsequently, a nitrogen gas of 30 mL min<sup>-1</sup> was purged for 2 h to exclude oxygen gas prior to heating. The autoclave was sealed and heated in an oven at 473 K for different times under autogenous pressure. After

cooled naturally, the products were centrifuged, washed with deionized water and dried at 333 K in an oven. The samples were denoted as SN-n-m (n is the reaction time and m is the reaction pH value), for example, sample SN-48-2 meant that the sample prepared for 48 h under pH 2. As a comparison, bulk SnNb<sub>2</sub>O<sub>6</sub> (defined as SN-SSR) was prepared by a traditional solid reaction using Sn<sub>3</sub>(OH)<sub>2</sub>O<sub>2</sub> as a precursor based on earlier work.<sup>34, 35</sup> N-doped TiO<sub>2</sub> was prepared following our previous work.<sup>40</sup>

### 2.2. Characterization

The X-ray diffraction (XRD) measurements were performed on a Bruker D8 Advance X-ray diffractometer using Cu K<sub>α1</sub> radiation (λ = 1.5406 Å). Thermogravimetric (TG) analysis was performed on TG209 (NETZSCH Co.). Transmission electron microscopy (TEM) images were recorded using a JEOL model JEM 2010 EX microscope at an accelerating voltage of 200 kV. A tapping-mode atomic force microscopy (AFM, Nanoscope Multimode IIIa, Veeco Instruments) with Si-tip cantilever was used to evaluate the morphology and the thickness of the obtained samples on the mica substrate. The Brunauer–Emmett–Teller (BET) surface area and the CO<sub>2</sub> adsorption were measured with an ASAP2020M apparatus (Micromeritics Instrument Corp., USA). The nitrogen adsorption and desorption isotherms were measured at 77 K, and CO<sub>2</sub> adsorption isotherms were measured at 273 K. UV-vis diffuse reflection spectra (UV-vis DRS) of the samples were recorded on a Varian Cary-500 spectrophotometer. CO<sub>2</sub> temperature-programmed desorption (CO<sub>2</sub> TPD) were carried out using a Micromeritics AutoChem II 2920 instrument. In-situ CO-adsorbed fourier transform infrared (FTIR) spectra were performed in a home-made IR cell in conjunction with a vacuum system on a Nicolet 670 FTIR spectrometer at a resolution of 4 cm<sup>-1</sup> and 32 scans.<sup>14</sup>

### 2.3. Electrochemistry measurement

The fluorine-doped tin oxide (FTO) glasses, as working electrode, were cleaned by sonication in cleanout fluid, acetone and ethanol for 10 min, respectively. 5 mg photocatalyst powder was dispersed into 0.5 ml dimethylformamide under sonication for 6 h to get slurry. The as-prepared slurry spread onto the conductive surface of FTO glass to form a photocatalyst film with the area of 0.25 cm<sup>2</sup>. Subsequently, uncoated parts of the FTO glass were isolated with epoxy resin.

Photocurrent was measured by the conventional three-electrode electrochemical cell with a working electrode, a platinum foil counter electrode and a saturated Ag/AgCl electrode as reference electrode. The working electrode was immersed in a sodium sulfate electrolyte solution (0.2 M) and irradiated by a 300 W Xe lamp (λ = 420–780 nm). The light/dark short circuit photocurrent response was recorded with a BAS Epsilon workstation. For current polarity, the cathodic current was set as positive current.

### 2.4. Evaluation of photocatalytic activity

The photocatalytic reduction of CO<sub>2</sub> was performed in a 40 mL Schlenk flask at ambient temperature and atmospheric pressure. The reactor was sealed with a silicone rubber

septum. The light source was a 300 W Xe lamp with a cut-off filter to occlude light below 420 nm. The photocatalytic reaction was performed in a gas-solid heterogeneous reaction mode. In a typical photocatalytic experiment, 20 mg solid photocatalyst was placed in the reactor. This system was subjected to vacuum degassing and then backfilling with pure CO<sub>2</sub> gas. This process was repeated three times, and after the last cycle, the flask was backfilled with CO<sub>2</sub> (1 bar). 6 μL of liquid water was introduced into the flask with a syringe via the septum. Then liquid water was turned in gaseous water, in order to ensure that the catalyst was surrounded by H<sub>2</sub>O vapor and CO<sub>2</sub>. The temperature of the reactor was kept at 298 K. The photocatalytic reaction was typically carried out for 4 h. 0.5 mL of gas was taken from the reactor to analyze the gas concentration of the product using a gas chromatography (GC-7890A, Agilent) equipped with a flame ionized detector (FID). Product gases were calibrated with the standard gas mixtures and their identity determined using the retention time.

### 3. Results and discussion

#### 3.1. Structural features

The crystallinity and crystal phase for the as-prepared products were confirmed by XRD measurements, as shown in Fig. 1. It is clear that the diffraction peaks can be exactly indexed to the standard SnNb<sub>2</sub>O<sub>6</sub> phase (JCPDS: 84-1810; Monoclinic phase; Space group: C2/c). No impurity peaks from other phases can be detected over the SN-48-2 and SN-48-4 samples. However, some unreacted SnO<sub>2</sub> were found on the SN-12-2, SN-24-2 and SN-48-6 samples. Notably, as the reaction time is prolonged, the sample's crystallinity increases. Furthermore, the crystallinities of the samples are also sensitive to the pH value of the reaction system. With increasing the pH values, the crystallinity of the sample is decreased. That is, the optimal conditions of SnNb<sub>2</sub>O<sub>6</sub> are prepared at 473 K for 48 h under pH 2. The average crystallite size is estimated based on the peak at 2θ = 24.8° using the Scherrer equation. As shown in Table 1, the calculated crystal sizes of the samples prepared by hydrothermal reaction are about 10 nm, while the crystal size of the sample prepared by traditional solid state reaction is over 80 nm.

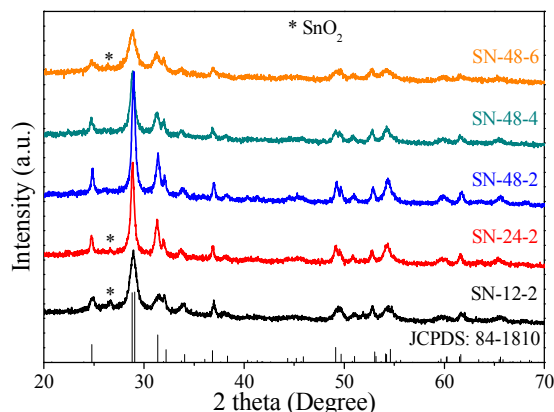


Fig. 1 XRD patterns of the as-prepared samples

As the instability of Sn<sup>2+</sup>, the pure SnNb<sub>2</sub>O<sub>6</sub> is difficult to be prepared. To further confirm the compositions of the as-prepared samples, thermogravimetric analyses were carried out in air and high-pure He atmospheres to judge whether Sn<sup>2+</sup> in SnNb<sub>2</sub>O<sub>6</sub> was oxidized to Sn<sup>4+</sup> in the preparation process. When pure SnNb<sub>2</sub>O<sub>6</sub> was oxidized by oxygen into SnO<sub>2</sub> and Nb<sub>2</sub>O<sub>5</sub>, the weight of the product would increase 5% according to the equation: Sn<sup>(II)</sup>Nb<sub>2</sub>O<sub>6</sub> + 1/2O<sub>2</sub> = Sn<sup>(IV)</sup>O<sub>2</sub> + Nb<sub>2</sub>O<sub>5</sub>. As shown in Fig. 2, when the SN-48-2 sample was calcined under high-pure He atmosphere, the weight of SN-48-2 was decreased gradually with increasing the temperature. This could be ascribed to the loss of adsorbed H<sub>2</sub>O. However, when the SN-48-2 sample was calcined under air atmosphere, its weight was gained and then reduced. This is due to the fact that the oxidation of Sn<sup>2+</sup> to Sn<sup>4+</sup>. The difference of the loss weight of the samples annealed under air and He is about 5%, which well matches with the theoretical value. That is, SN-48-2 sample would be a pure SnNb<sub>2</sub>O<sub>6</sub> sample.

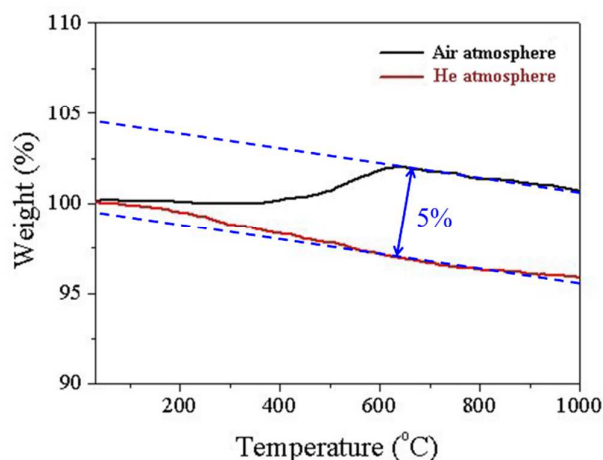


Fig. 2 TG analysis of the SN-48-2 sample under air and He atmospheres (heating rate of 5 °C per minute)

#### 3.2 Morphology

The morphologies and microstructures of the samples were investigated by TEM and AFM. As shown in Fig. 3a and b, both SN-48-2 and SN-48-4 are composed of numerous irregular nanosheets (NSs). The lateral scales of the nanosheets range from several hundred nanometers to several micrometers. It should be pointed out that the SN-48-2 NSs exhibit nearly transparent feature, indicating the ultrathin thickness (Fig. 3a). In contrast, SN-48-4 NSs are thicker than SN-48-2 (Fig. 3e and Fig. S1). This may be ascribed to the low pH value of reaction system facilitating the dissolution-recrystallization of  $\text{SnNb}_2\text{O}_6$  in the preparation process.<sup>36</sup> As a result, the thickness of the nanosheets would definitely reduce. Due to the features of 2D nanosheet, the BET surface areas of the  $\text{SnNb}_2\text{O}_6$  nanosheets are estimated over  $45 \text{ m}^2 \text{ g}^{-1}$ , which is about 35 times larger than that of layered  $\text{SnNb}_2\text{O}_6$  ( $1.3 \text{ m}^2 \text{ g}^{-1}$ ), as shown in Table 1. The large surface area could provide more reactive sites and adsorb more reactants. Fig. 3c

shows the typical high-resolution TEM image of SN-48-2. Clear lattice fringes can be observed. The interplanar spacing is consistent with the  $d$ -spacing of the corresponding lattice plane. The fringes of  $d = 0.28 \text{ nm}$  and  $d = 0.37 \text{ nm}$  match well with that of the (002) and (310) crystallographic plane of monoclinic  $\text{SnNb}_2\text{O}_6$ , respectively. A typical selected area electron diffraction (SAED) pattern of the SN-48-2 NSs reveals that the sample has single-crystalline character and high crystallinity (Fig. 3d). The superb crystal quality excludes the possibility of any grain boundaries and/or other interfaces (which usually act as recombination sites in polycrystalline materials). This should favor improved separation of the photogenerated electron and hole and decrease the electron-hole recombination rate. The thickness of the SN-48-2 NSs is further confirmed by AFM analysis that reveals a thickness of approximately  $1 \text{ nm}$  (Fig. 3e). This thickness is in agreement with the theoretical value of monolayer  $\text{SnNb}_2\text{O}_6$  ( $0.8 \text{ nm}$ ).<sup>36, 37</sup>

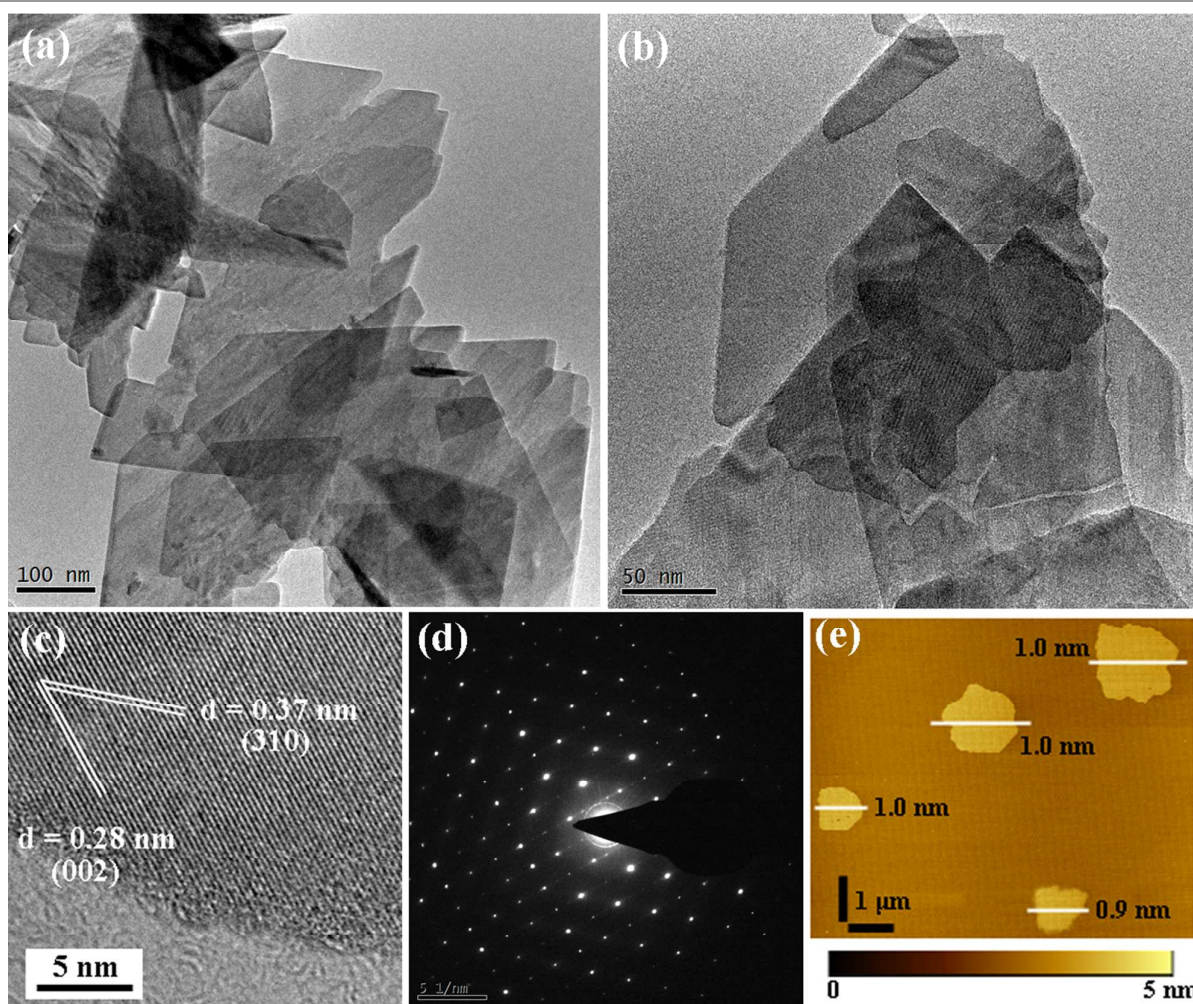


Fig. 3 TEM (a, b), HRTEM images (c), SAED pattern (d), and AFM image (e) of SN-48-2 (a, c-e) and SN-48-4 (b)



## Journal Name

## ARTICLE

**Table 1** Average crystallite size, surface area, CO<sub>2</sub> adsorption capability and CH<sub>4</sub> production rate of the samples

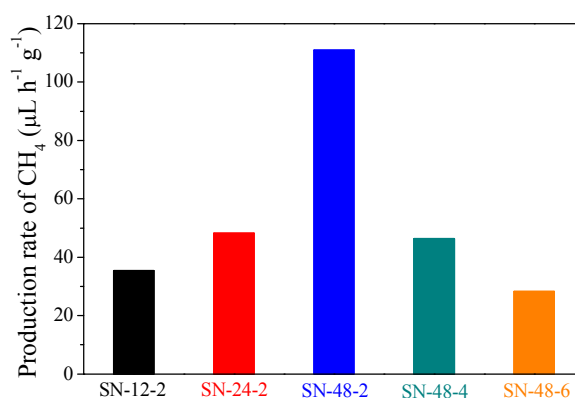
Sample	Average crystallite size (nm)	A <sub>BET</sub> <sup>a</sup> (m <sup>2</sup> g <sup>-1</sup> )	C <sub>CO<sub>2</sub></sub> <sup>b</sup> (cm <sup>3</sup> g <sup>-1</sup> )	C <sub>CO<sub>2</sub></sub> <sup>c</sup> (cm <sup>3</sup> m <sup>-2</sup> )	R <sub>CH<sub>4</sub></sub> <sup>d</sup> (μL h <sup>-1</sup> g <sup>-1</sup> )	R <sub>CH<sub>4</sub></sub> <sup>e</sup> (μL h <sup>-1</sup> m <sup>-2</sup> )
SN-12-2	9.1	36.6	8.6	0.235	35.39	0.9632
SN-24-2	12.6	40.9	10.7	0.262	48.16	1.165
SN-48-2	13.9	45.6	13.5	0.296	110.9	2.442
SN-48-4	11.0	34.2	10.0	0.292	46.37	1.366
SN-48-6	8.3	31.2	6.8	0.218	28.22	0.896
SN-SSR	80.5	1.3	0.3	0.231	9.408	7.235

<sup>a</sup> A<sub>BET</sub> surface area; <sup>b</sup> Adsorbed capacity of CO<sub>2</sub> at a pressure of 1 bar; <sup>c</sup> CO<sub>2</sub> adsorbed capacity normalized with surface area; <sup>d</sup> Production rate of CH<sub>4</sub>; <sup>e</sup> Production rate of CH<sub>4</sub> normalized with surface area.

### 3.3 Photocatalytic activity

The photocatalytic activities of the as-prepared samples have been evaluated by the reduction of CO<sub>2</sub> in the gaseous phase at 298 K under visible light irradiation. Since the minimum conduction band potential of SnNb<sub>2</sub>O<sub>6</sub> (-1.0 V vs NHE)<sup>37</sup> is more negative than the reduction potential of CO<sub>2</sub>/CH<sub>4</sub> (-0.24 V vs NHE),<sup>14</sup> and the maximum valence band of SnNb<sub>2</sub>O<sub>6</sub> (+1.6 V vs NHE)<sup>37</sup> is more positive than that of the oxidation potential of H<sub>2</sub>O/H<sup>+</sup> (+0.82 V vs NHE),<sup>7</sup> it is energetically favourable for reaction of the photogenerated electrons and holes from SnNb<sub>2</sub>O<sub>6</sub> with adsorbed CO<sub>2</sub> and H<sub>2</sub>O to initiate the reduction of CO<sub>2</sub>, producing CH<sub>4</sub>. Fig. 4 shows the production rate of the as-prepared SnNb<sub>2</sub>O<sub>6</sub> nanosheet samples under visible light irradiation. It can be seen that all of the samples show obvious photocatalytic activities for the reduction of CO<sub>2</sub> with H<sub>2</sub>O into CH<sub>4</sub>. The productive gas analysis shows no any other hydrocarbon product, such as CH<sub>3</sub>OH, CH<sub>3</sub>CH<sub>3</sub> etc. Among the SnNb<sub>2</sub>O<sub>6</sub> nanosheet samples, the activities of the samples are influenced by the preparation conditions (pH value and reaction time). The activity follows the order: SN-48-2 > SN-24-2 > SN-48-4 > SN-12-2 > SN-48-6. The CH<sub>4</sub> formation rate of SN-48-2 reaches 110.9 μL h<sup>-1</sup> g<sup>-1</sup>. Moreover, the SN-48-2 sample exhibits a high stability of the photocatalytic activity. There is no obvious decrease in activity during the recycling experiments (Fig. S2). To further find out the main factors accounting for different photocatalytic activities, we normalized the CH<sub>4</sub> production rates with the surface areas to rule out the effect of surface areas on their photocatalytic activities (Table 1). After comparing the reduction rates of CO<sub>2</sub> before and after normalizing with the surface areas, we find that the order of the normalized rates of the SnNb<sub>2</sub>O<sub>6</sub> nanosheet samples is similar with that of the original ones. The high crystallinity and purity of SnNb<sub>2</sub>O<sub>6</sub>

should be another important factor to improve photocatalytic efficiency.

**Fig. 4** Photocatalytic activities of the as-prepared SnNb<sub>2</sub>O<sub>6</sub> nanosheet samples

Considering that CO, H<sub>2</sub>, and O<sub>2</sub> may be formed during the photocatalytic reduction of CO<sub>2</sub>, we measured the amount of these products through a gas chromatography equipped with thermal conductivity detector (TCD). As shown in Table S1, these products are found on all the samples. Only few CO<sub>2</sub> was reduced into CO. Among the as-prepared samples, pure SnNb<sub>2</sub>O<sub>6</sub> nanosheets facilitate the formation of CH<sub>4</sub> and the formation of H<sub>2</sub> has been suppressed. This may be due to the unique features and the open structure of 2D nanosheet. However, the existence of SnO<sub>2</sub> may enhance the formation rate of H<sub>2</sub>. This may be because some of photogenerated electrons transfer from SnNb<sub>2</sub>O<sub>6</sub> to SnO<sub>2</sub> and SnO<sub>2</sub> benefits to the formation of H<sub>2</sub> compared with SnNb<sub>2</sub>O<sub>6</sub>. For O<sub>2</sub>, we find that the amount of O<sub>2</sub> increased with reaction time over the

as-prepared samples, although the molar ratio of  $2\text{O}_2/(\text{CO} + 4\text{CH}_4 + \text{H}_2)$  is lower than the stoichiometric ratio (1: 1). This may be attributed to the formation of other oxidation products over the surface of the samples. We will deeply investigate them in our further work.

Furthermore, a set of control experiments were carried out to confirm the photocatalytic process in the photoreduction of  $\text{CO}_2$ . As shown in Fig. 5, the reduction of  $\text{CO}_2$  could be negligible in the absence of either photocatalysts or visible light. Additionally, to rule out the possibilities of residual carbon for  $\text{CH}_4$  yield during reaction process, the SN-48-2 nanosheets were illuminated with  $\text{N}_2$  as the carrier gas without input of  $\text{CO}_2$ . It can be clearly found that there is an inactivation in  $\text{N}_2$  atmosphere, indicating that the generated  $\text{CH}_4$  indeed originates from photoreduction of  $\text{CO}_2$ . For reference, a  $\text{SnNb}_2\text{O}_6$  sample prepared by a solid state reaction (SN-SSR) and a common N-doped  $\text{TiO}_2$  (N- $\text{TiO}_2$ ) photocatalyst were also tested for the photoreduction of  $\text{CO}_2$  under the same conditions. Notably, the  $\text{CH}_4$  evolution rates over SN-SSR and N- $\text{TiO}_2$  are only  $9.408$  and  $28 \mu\text{L h}^{-1} \text{g}^{-1}$ , respectively, which are much lower than that over SN-48-2. Considering that the surface area of SN-48-2 is higher than SN-SSR, the higher activity of SN-48-2 may be ascribed to the strong  $\text{CO}_2$  gas adsorption ability and more reaction sites arising from high specific surface area offered by the nanosheets. In addition, ultrathin geometry of the nanosheet is also favorable for charge carriers for fast mobility from the interior onto the surface to participate in the photoreduction reaction.

To verify  $\text{CH}_4$  formation resulting from  $\text{CO}_2$  reduction, isotope tracer analyses involving  $^{13}\text{CO}_2$  were conducted for SN-48-2 sample. Fig. S3 shows the mass chromatography spectra for visible light-irradiated  $\text{SnNb}_2\text{O}_6$  nanosheets under different atmospheres. Under  $^{13}\text{CO}_2$  atmosphere,  $\text{CH}_4$  molecules are mainly composed of  $^{13}\text{CH}_4$  ( $m/e = 17$ ). While,  $^{12}\text{CH}_4$  ( $m/e = 16$ ) are the major product under  $^{12}\text{CO}_2$  atmosphere. Furthermore, when the experiment was carried out under  $\text{N}_2$  atmosphere, the yields of  $^{13}\text{CH}_4$  and  $^{12}\text{CH}_4$  could be ignored. Therefore, we could conclude that the formation of  $\text{CH}_4$  derives from the reduction of  $\text{CO}_2$ .

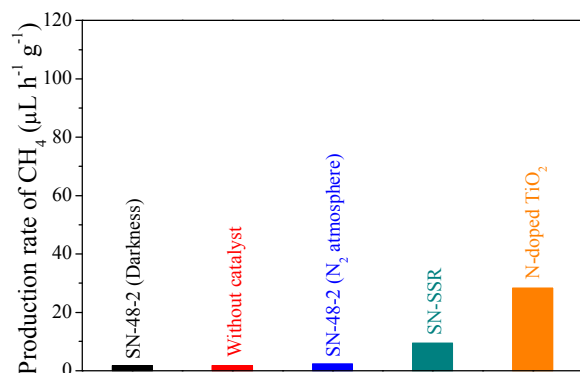


Fig. 5 Controlled experiments on the reduction of  $\text{CO}_2$  over SN-48-2 and the photocatalytic activities of the reference (layered  $\text{SnNb}_2\text{O}_6$  and N-doped  $\text{TiO}_2$ )

### 3.4 Photoabsorption performance

As the photoabsorption property plays a crucial role in determining the photocatalytic activity, the UV-vis diffuse reflectance spectra of the samples were recorded (Fig. 6). Obviously, the samples have a strong absorption in the visible light region. The wavelength at the absorption edge,  $\lambda$ , is determined as the intercept on the wavelength axis for a tangent line drawn on the absorption spectra. The samples have a similar photoabsorption edge, which locates at about  $477 \text{ nm}$ . The optical band gaps of the samples estimated from the Kubelka–Munk function are approximately  $2.6 \text{ eV}$ . The photoabsorption in the wavelength range of  $477\text{--}560 \text{ nm}$  may be caused by the surface defects (Fig. S4). Notably, the SN-48-2 sample exhibits a less pronounced background level of the absorption at the same position among the as-prepared samples, indicating SN-48-2 with lower surface defect sites. Furthermore, in the UV region, the samples with the impurity of  $\text{SnO}_2$  show two absorption peaks. One is contributed by the absorption of  $\text{SnO}_2$  and the other is attributed to the absorption of  $\text{SnNb}_2\text{O}_6$ . However, the SN-48-2 and SN-48-4 samples just exhibit one absorption peak. The existence of the impurity may enhance the photoabsorption performance in the UV region. These results confirm that the difference in photocatalytic activities of the samples do not derive from the difference of photoabsorption performance.

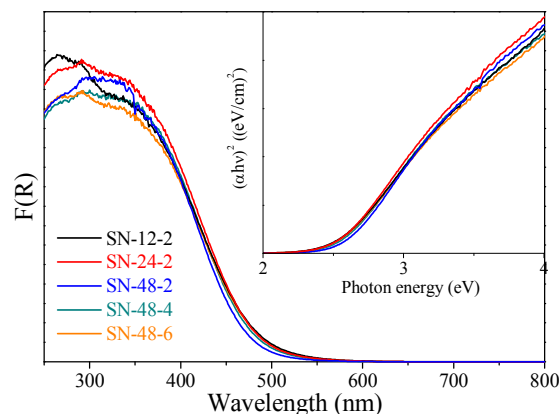


Fig. 6 UV-vis DRS of the as-prepared samples

### 3.5 Photoelectric performance

We further utilized the transient photocurrent responses experiments at a bias potential of  $0 \text{ V}$  to investigate the electron generation and the charge carrier transport characteristics of the as-prepared samples (Fig. 7). Initially, steady currents are observed without illumination. Once the light was turned on, the current rapidly increases and immediately reaches the steady state. As the Xe lamp is switched off, the current returns to the initial value, showing good reversibility of the process. It is clear that the increased photoresponse current is considerably larger on SN-48-2 than on other samples, suggesting that many more electrons could be photogenerated by SN-48-2. According to Fig. 7, the steady

photocurrent densities of SN-12-2, SN-24-2, SN-48-2, SN-48-4, and SN-48-6 are about 26.3, 35.2, 72.0, 50.1, and 10.7, respectively. The order of photocurrent density is consistent with that of the photocatalytic activity. Thus, we can also ascribe the enhancement of photocatalytic performance over SN-48-2 to the increased concentration of photogenerated electrons and a better electron transfer rate.

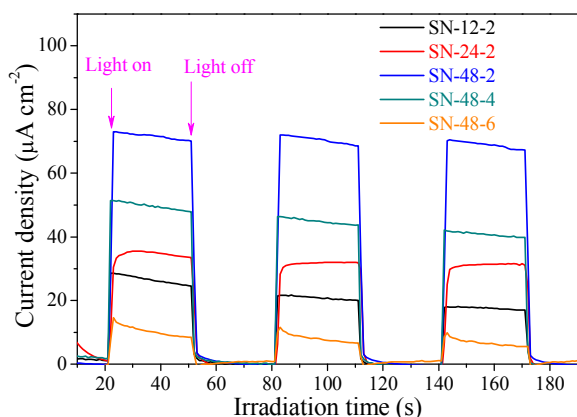


Fig. 7 Short-circuit photocurrent response of SnNb<sub>2</sub>O<sub>6</sub> prepared at different conditions in a 0.2 M Na<sub>2</sub>SO<sub>4</sub> aqueous electrolyte under visible light irradiation

### 3.6 CO<sub>2</sub> adsorption property

It is considered that the mass transfer of CO<sub>2</sub> on the photocatalyst is a preceding step in its photoreduction and the surface adsorption state of CO<sub>2</sub> plays a key role in affecting the activation of CO<sub>2</sub>.<sup>41</sup> Firstly, the CO<sub>2</sub> adsorption isotherms of the SN-SSR and the SnNb<sub>2</sub>O<sub>6</sub> nanosheet samples were tested to study CO<sub>2</sub> adsorption ability, as shown in Table 1. Due to their high specific surface areas, it is expected that the CO<sub>2</sub> adsorption capacities of SnNb<sub>2</sub>O<sub>6</sub> nanosheet samples are much higher than that of SN-SSR sample. Such an increased CO<sub>2</sub> concentration on the nanosheets' surface is beneficial for enhancing the mass transfer efficiency of CO<sub>2</sub> and then increasing the photocatalytic activity. The maximum CO<sub>2</sub> uptake for SN-48-2 is about 13.5 cm<sup>3</sup> g<sup>-1</sup> at the pressure of 1 bar, which is 45 times of that over SN-SSR. By normalizing with respect to surface area, we can see that the CO<sub>2</sub> adsorption capacities over the SnNb<sub>2</sub>O<sub>6</sub> samples are similar.

The temperature-programmed desorption of CO<sub>2</sub> (CO<sub>2</sub>-TPD) was further carried out to investigate the interaction of CO<sub>2</sub> and the catalysts, and the curves are given in Fig. 8. In the TPD profile of CO<sub>2</sub> adsorbed on SN-48-2, the strong desorption peaks of CO<sub>2</sub> at temperatures between 50 and 600 °C are observed. The TPD signal peak of CO<sub>2</sub> at about 100 °C may be attributed to the interaction between CO<sub>2</sub> and the weak basic sites presented in SN-48-2.<sup>42</sup> The desorption peaks occurring at about 400 °C were due to the presence of moderate basic sites.<sup>43</sup> Moreover, the desorption peaks present at above 500 °C may be corresponded to strong basic sites.<sup>42</sup> In contrast, the TPD result for SN-SSR sample shows only two weak desorption peaks at 400 and 500 °C, respectively. The concentration of

alkaline sites could be estimated by the total area under the curve for all the desorption peaks. It is clear that the total basicity of SN-48-2 is much larger than SN-SSR. The higher concentration of basic sites and CO<sub>2</sub> absorption ability in the SN-48-2 sample may be related to its high surface area and ultrathin nanosheet structure. The result could also explain the enhanced photocatalytic activity of SN-48-2.

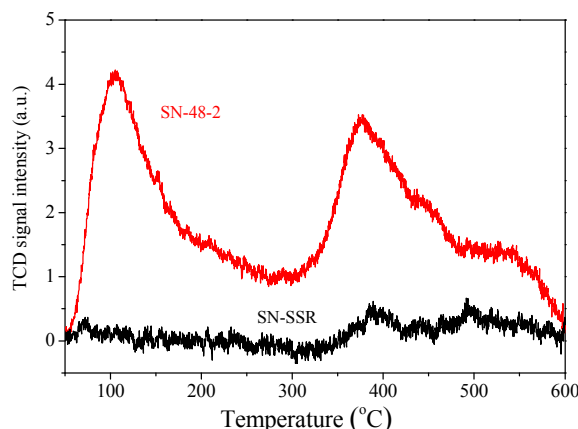


Fig. 8 CO<sub>2</sub>-TPD for the SN-48-2 and SN-SSR samples

### 3.7 Surface chemistry and reaction intermediates

For the gaseous phase CO<sub>2</sub> photoreaction, the interaction between the CO<sub>2</sub> molecule and the surface of photocatalyst is the important and initial step.<sup>44</sup> Four carbon-containing species (CO<sub>2</sub><sup>-</sup>, HCO<sub>3</sub><sup>-</sup>, monodentate carbonate (m-CO<sub>3</sub><sup>2-</sup>) and bidentate carbonate (b-CO<sub>3</sub><sup>2-</sup>)) were considered as the primary intermediates on the surfaces during the CO<sub>2</sub> photoreduction process.<sup>14, 45-47</sup> To identify the surface adsorption state of CO<sub>2</sub> and active intermediates on the as-prepared SnNb<sub>2</sub>O<sub>6</sub> nanosheet, the in situ FTIR analysis was carried out. Fig. 9 shows the typical in situ FTIR spectra of CO<sub>2</sub> and H<sub>2</sub>O co-interaction with SN-48-2 before and after visible light irradiation. A number of absorption peaks in the range of 1800-1000 cm<sup>-1</sup> are observed when CO<sub>2</sub> and H<sub>2</sub>O were co-adsorbed on the surface of SnNb<sub>2</sub>O<sub>6</sub> after the adsorption-desorption equilibrium. A weak and wide absorption peak at 1055 cm<sup>-1</sup> is assigned to b-CO<sub>3</sub><sup>2-</sup>. Two very weak peaks at 1410 and 1460 cm<sup>-1</sup> are attributed to the surface m-CO<sub>3</sub><sup>2-</sup> and HCO<sub>3</sub><sup>-</sup> species, respectively. A clear adsorbed H<sub>2</sub>O feature at 1629 cm<sup>-1</sup> can also be found on the surface of SnNb<sub>2</sub>O<sub>6</sub> nanosheets. Furthermore, a sharp peak, located at 1250 cm<sup>-1</sup>, is corresponded to the carboxylate (CO<sub>2</sub><sup>-</sup>) species. The formation of CO<sub>2</sub><sup>-</sup> indicates that an electron could be spontaneously attached to CO<sub>2</sub> from the nanosheets even in the dark. It should be noted that CO<sub>2</sub> is a rather inert molecule with a positive electron affinity and the process CO<sub>2</sub> + e<sup>-</sup> = ·CO<sub>2</sub><sup>-</sup> is an energetically unfavorable reaction. The electron-rich surface of the nanosheets facilitates the chemical adsorption of CO<sub>2</sub> molecules to form the active species. These active CO<sub>2</sub> species will reduce the activation energy of photocatalytic CO<sub>2</sub> reduction, and thus the photocatalytic activity will be

obviously increased. Under subsequent visible light illumination for 60 min, the intensity of the absorption peaks of  $\text{H}_2\text{O}$  and  $\text{CO}_2^-$  are significantly decreased. These spectral changes in Fig. 9 suggest that the  $\text{CO}_2^-$  species may be the predominant intermediate on our sample's surface during the  $\text{CO}_2$  photoreduction process, and  $\text{H}_2\text{O}$  participates in the reaction with  $\text{CO}_2$  by donating electrons or scavenging holes. In contrast, the FTIR features for  $\text{m-CO}_3^{2-}$ ,  $\text{b-CO}_3^{2-}$  and  $\text{HCO}_3^-$  species are almost identical to those in the dark, indicating that these species may not be active species for  $\text{CO}_2$  reduction into  $\text{CH}_4$  on  $\text{SnNb}_2\text{O}_6$  nanosheets. It is worth noting that these species are very little on our  $\text{SnNb}_2\text{O}_6$  nanosheets and most of the adsorbed  $\text{CO}_2$  species are reactive  $\text{CO}_2^-$  species. Surface accumulated non-reactive  $\text{CO}_3^{2-}$  species ( $\text{m-CO}_3^{2-}$  and  $\text{b-CO}_3^{2-}$ ) may lead to the deactivation of photocatalysts.<sup>48</sup> Therefore, this is may be another reason for our  $\text{SnNb}_2\text{O}_6$  nanosheets with high photocatalytic activity.

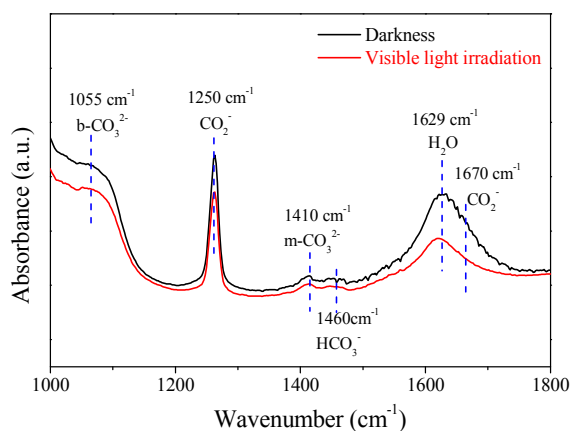


Fig. 9 In situ FTIR spectra of  $\text{CO}_2$  and  $\text{H}_2\text{O}$  interaction with SN-48-2 in the darkness and subsequently irradiated by visible light

### 3.8 Mechanism of $\text{CO}_2$ photoreduction with $\text{H}_2\text{O}$

Based on the above experimental results and analysis, a possible mechanism for the photocatalytic reduction of  $\text{CO}_2$  to  $\text{CH}_4$  over  $\text{SnNb}_2\text{O}_6$  nanosheets under visible light irradiation is proposed, and is illustrated in Fig. 10. Firstly,  $\text{CO}_2$  and  $\text{H}_2\text{O}$  molecules are strongly adsorbed onto the surface of  $\text{SnNb}_2\text{O}_6$  nanosheets due to the unique 2D nanosheet structure feature and the basicity of surface. The chemisorbed  $\text{CO}_2$  molecule becomes destabilized to form "Sn- $\text{CO}_2$ " surface complex species and its reactivity is believed to be higher than that of the free  $\text{CO}_2$  molecule. Under visible light irradiation, a band-to-band charge transfer on  $\text{SnNb}_2\text{O}_6$  nanosheets would take place and the charge carrier would separate and migrate rapidly from the interior to the surface to participate in the photoreduction reaction due to the ultrathin geometry of the nanosheet. The photoexcited electrons promote the reduction of adsorbed hydroxyl species to form atomic hydrogen on the surface of the nanosheet. At the same time, the photogenerated holes ( $\text{h}^+$ ) may be quenched by the oxidation of another adsorbed hydroxyl species. Notably, the adsorbed

$\text{CO}_2$  molecules may also be activated by photogenerated electrons. Finally, the activated  $\text{CO}_2$  species would transform into  $\text{CH}_4$  through reacting with the formed atomic hydrogen on the surface of  $\text{SnNb}_2\text{O}_6$  nanosheets via a photogenerated electron-induced multistep reduction process involving electron and proton transfer, C-O bond breaking, and C-H bond formation. Because the formed  $\text{CH}_4$  has a poor interaction with the photocatalyst,  $\text{CH}_4$  could be desorbed fast without degrading.

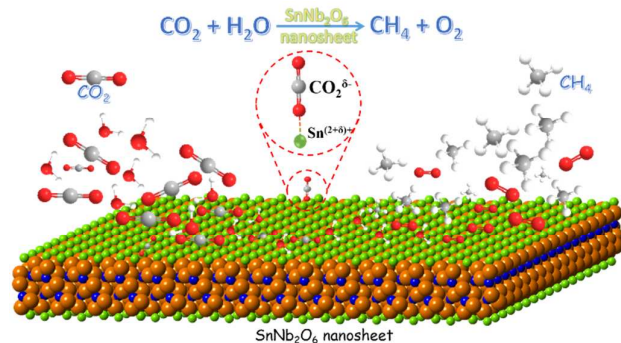


Fig. 10 Schematic of photocatalytic reduction of  $\text{CO}_2$  on  $\text{SnNb}_2\text{O}_6$  2D nanosheets

## Conclusions

In summary, ultrathin  $\text{SnNb}_2\text{O}_6$  2D nanosheets have been successfully prepared by a simple hydrothermal method without any organic additives. These ultrathin  $\text{SnNb}_2\text{O}_6$  nanosheets are applied into photocatalytic reduction of  $\text{CO}_2$  with  $\text{H}_2\text{O}$  to  $\text{CH}_4$  for the first time and show efficient activity under visible light irradiation. The photocatalytic activity of  $\text{SnNb}_2\text{O}_6$  nanosheets is significantly influenced by the crystallinity, the purity, the surface area, the photoelectric performance and the basicity of the surface. By optimizing these effects, the as-prepared SN-48-2 samples exhibits the highest  $\text{CH}_4$  evolution rate ( $110.9 \mu\text{L h}^{-1} \text{g}^{-1}$ ). We believe that the present study will widen the application of the 2D nanosheet and stimulate intensive research in the utilization of the 2D nanosheet for the photocatalytic conversion of  $\text{CO}_2$  to valuable hydrocarbons using solar energy.

## Acknowledgements

The work is financially supported by National Natural Science Foundation of China (Grants No. 21303019, 21177024, U1305242), the Natural Science Foundation of Fujian Province (Grants No. 2014J05016), China Postdoctoral Science Foundation (Grants No. 2015M571964) and Hong Kong Scholars Program (XJ2014050).

## Notes and references

- § Corresponding author: Dr. Shijing Liang; E-mail: [sjliang2011@gmail.com](mailto:sjliang2011@gmail.com); Tel & Fax: 86-591-22866070  
 §§ Corresponding author: Prof. Dr. Xuxu Wang; E-mail: [xwang@fzu.edu.cn](mailto:xwang@fzu.edu.cn); Tel & Fax: 86-591-83779251

- 1 P. D. Tran, L. H. Wong, J. Barber and J. S. C. Loo, *Energy Environ. Sci.*, 2012, **5**, 5902-5918.
- 2 J. Mao, K. Li and T. Peng, *Catal. Sci. Technol.*, 2013, **3**, 2481-2498.
- 3 Y. Oh and X. Hu, *Chem. Soc. Rev.*, 2013, **42**, 2253-2261.
- 4 S. N. Habisreutinger, L. Schmidt-Mende and J. K. Stolarczyk, *Angew. Chem. Int. Ed.*, 2013, **52**, 7372-7408.
- 5 X. Li, J. Wen, J. Low, Y. Fang and J. Yu, *Sci. China Mater.*, 2014, **57**, 70-100.
- 6 H. Shi, T. Wang, J. Chen, C. Zhu, J. Ye and Z. Zou, *Catal. Lett.*, 2011, **141**, 525-530.
- 7 Q. Liu, Y. Zhou, J. Kou, X. Chen, Z. Tian, J. Gao, S. Yan and Z. Zou, *J. Am. Chem. Soc.*, 2010, **132**, 14385-14387.
- 8 S. C. Yan, S. X. Ouyang, J. Gao, M. Yang, J. Y. Feng, X. X. Fan, L. J. Wan, Z. S. Li, J. H. Ye, Y. Zhou and Z. G. Zou, *Angew. Chem. Int. Ed.*, 2010, **49**, 6400-6404.
- 9 Q. Li, X. Li, S. Wageh, A. A. Al-Ghamdi and J. Yu, *Adv. Energy Mater.*, 2015, **5**, 1500010.
- 10 T. Inoue, A. Fujishima, S. Konishi and K. Honda, *Nature*, 1979, **277**, 637-638.
- 11 M. Anpo, H. Yamashita, Y. Ichihashi and S. Ehara, *J. Electroanal. Chem.*, 1995, **396**, 21-26.
- 12 V. P. Indrakanti, J. D. Kubicki and H. H. Schobert, *Energy Environ. Sci.*, 2009, **2**, 745-758.
- 13 J. Yu, J. Low, W. Xiao, P. Zhou and M. Jaroniec, *J. Am. Chem. Soc.*, 2014, **136**, 8839-8842.
- 14 S. Zhu, S. Liang, Y. Tong, X. An, J. Long, X. Fu and X. Wang, *Phys. Chem. Chem. Phys.*, 2015, **17**, 9761-9770.
- 15 J.-Y. Liu, B. Garg and Y.-C. Ling, *Green Chem.*, 2011, **13**, 2029-2031.
- 16 J. Lin, Z. Pan and X. Wang, *ACS Sustainable Chem. Eng.*, 2014, **2**, 353-358.
- 17 J. Lin, Z. Ding, Y. Hou and X. Wang, *Sci. Rep.*, 2013, **3**, 1056.
- 18 S. Cao, J. Low, J. Yu and M. Jaroniec, *Adv. Mater.*, 2015, **27**, 2150-2176.
- 19 R. Kuriki, K. Sekizawa, O. Ishitani and K. Maeda, *Angew. Chem. Int. Ed.*, 2015, **54**, 2406-2409.
- 20 Y. Fu, D. Sun, Y. Chen, R. Huang, Z. Ding, X. Fu and Z. Li, *Angew. Chem. Int. Ed.*, 2012, **51**, 3364-3367.
- 21 S. Wang, W. Yao, J. Lin, Z. Ding and X. Wang, *Angew. Chem. Int. Ed.*, 2014, **53**, 1034-1038.
- 22 T. Zhang and W. Lin, *Chem. Soc. Rev.*, 2014, **43**, 5982-5993.
- 23 C.-C. Yang, J. Vernimmen, V. Meynen, P. Cool and G. Mul, *J. Catal.*, 2011, **284**, 1-8.
- 24 F. Sastre, A. V. Puga, L. Liu, A. Corma and H. García, *J. Am. Chem. Soc.*, 2014, **136**, 6798-6801.
- 25 K. Teramura, S. Iguchi, Y. Mizuno, T. Shishido and T. Tanaka, *Angew. Chem. Int. Ed.*, 2012, **51**, 8008-8011.
- 26 A. Bachmeier, S. Hall, S. W. Ragsdale and F. A. Armstrong, *J. Am. Chem. Soc.*, 2014, **136**, 13518-13521.
- 27 Y. Kou, Y. Nabetani, D. Masui, T. Shimada, S. Takagi, H. Tachibana and H. Inoue, *J. Am. Chem. Soc.*, 2014, **136**, 6021-6030.
- 28 P. Kumar, A. Bansawal, N. Labhsetwar and S. L. Jain, *Green Chem.*, 2015, **17**, 1605-1609.
- 29 D. Sun, W. Liu, Y. Fu, Z. Fang, F. Sun, X. Fu, Y. Zhang and Z. Li, *Chem. – Eur. J.*, 2014, **20**, 4780-4788.
- 30 Q. Zhai, S. Xie, W. Fan, Q. Zhang, Y. Wang, W. Deng and Y. Wang, *Angew. Chem. Int. Ed.*, 2013, **52**, 5776-5779.
- 31 F. Studt, I. Sharafutdinov, F. Abild-Pedersen, C. F. Elkjær, J. S. Hummelshøj, S. Dahl, I. Chorkendorff and J. K. Nørskov, *Nat. Chem.*, 2014, **6**, 320-324.
- 32 S. Navalón, A. Dhakshinamoorthy, M. Álvaro and H. Garcia, *ChemSusChem*, 2013, **6**, 562-577.
- 33 Y. Hosogi, K. Tanabe, H. Kato, H. Kobayashi and A. Kudo, *Chem. Lett.*, 2004, **33**, 28-29.
- 34 Y. Hosogi, H. Kato and A. Kudo, *Chem. Lett.*, 2006, **35**, 578-579.
- 35 Y. Hosogi, Y. Shimodaira, H. Kato, H. Kobayashi and A. Kudo, *Chem. Mater.*, 2008, **20**, 1299-1307.
- 36 S. Liang, S. Zhu, Y. Chen, W. Wu, X. Wang and L. Wu, *J. Mater. Chem.*, 2012, **22**, 2670-2678.
- 37 S. Liang, R. Liang, L. Wen, R. Yuan, L. Wu and X. Fu, *Appl. Catal. B*, 2012, **125**, 103-110.
- 38 L. P. Cruz, J. M. Savariault, J. Rocha, J. C. Jumas and J. D. Pedrosa de Jesus, *J. Solid State Chem.*, 2001, **156**, 349-354.
- 39 S. Liang, L. Wen, S. Lin, J. Bi, P. Feng, X. Fu and L. Wu, *Angew. Chem. Int. Ed.*, 2014, **53**, 2951-2955.
- 40 X. Chen, X. Wang, Y. Hou, J. Huang, L. Wu and X. Fu, *J. Catal.*, 2008, **255**, 59-67.
- 41 W. Tu, Y. Zhou and Z. Zou, *Adv. Mater.*, 2014, **26**, 4607-4626.
- 42 R. Song, D. Tong, J. Tang and C. Hu, *Energ. Fuel.*, 2011, **25**, 2679-2686.
- 43 S. Sato, R. Takahashi, M. Kobune and H. Gotoh, *Appl. Catal. A: Gen.*, 2009, **356**, 57-63.
- 44 L. Ye, J. Mao, T. Peng, L. Zan and Y. Zhang, *Phys. Chem. Chem. Phys.*, 2014, **16**, 15675-15680.
- 45 L. Liu, H. Zhao, J. M. Andino and Y. Li, *ACS Catal.*, 2012, **2**, 1817-1828.
- 46 J. Mao, L. Ye, K. Li, X. Zhang, J. Liu, T. Peng and L. Zan, *Appl. Catal. B*, 2014, **144**, 855-862.
- 47 P. Li, H. Xu, L. Liu, T. Kako, N. Umezawa, H. Abe and J. Ye, *J. Mater. Chem. A*, 2014, **2**, 5606-5609.
- 48 L. Liu, C. Zhao, H. Zhao, D. Pitts and Y. Li, *Chem. Commun.*, 2013, **49**, 3664-3666.

Graphical abstract:

**Photocatalytic reduction of CO<sub>2</sub> with H<sub>2</sub>O to CH<sub>4</sub> over ultrathin SnNb<sub>2</sub>O<sub>6</sub> 2D nanosheets under visible light irradiation**

Shuying Zhu,<sup>a</sup> Shijing Liang,<sup>a,b,c\*</sup> Jinhong Bi,<sup>a,b</sup> Minghua Liu,<sup>a,b</sup> Limin Zhou,<sup>c</sup> Ling Wu,<sup>a</sup> Xuxu

Wang<sup>a\*</sup>

*a* State Key Laboratory of Photocatalysis on Energy and Environment, Fuzhou University, Fuzhou 350002, P. R. China.

*b* Department of Environmental Science and Engineering, Fuzhou University, Minhou, Fujian, 350108, P. R. China.

*c* Department of Mechanical Engineering, The Hong Kong Polytechnic University, Hung Hom, Kowloon, Hong Kong

E-mail: sjliang2011@gmail.com (S. L.); xwang@fzu.edu.cn (X. W.)

